Microimaging of transient guest profiles to monitor mass transfer in nanoporous materials

Jörg Kärger[1]*, Tomas Binder[1], Christian Chmelik[1], Florian Hibbe[1], Harald Krautscheid[2], Rajamani Krishna[3] and Jens Weitkamp[4]

The intense interactions of guest molecules with the pore walls of nanoporous materials is the subject of continued fundamental research. Stimulated by their thermal energy, the guest molecules in these materials are subject to a continuous, irregular motion, referred to as diffusion. Diffusion, which is omnipresent in nature, influences the efficacy of nanoporous materials in reaction and separation processes. The recently introduced techniques of microimaging by interference and infrared microscopy provide us with a wealth of information on diffusion, hitherto inaccessible from commonly used techniques. Examples include the determination of surface barriers and the sticking coefficient's analogue, namely the probability that, on colliding with the particle surface, a molecule may continue its diffusion path into the interior. Microimaging is further seen to open new vistas in multicomponent guest diffusion (including the detection of a reversal in the preferred diffusion pathways), in guest-induced phase transitions in nanoporous materials and in matching the results of diffusion studies under equilibrium and non-equilibrium conditions.

The technological application of nanoporous materials, including mass separation[1–5], catalytic conversion[6–8], selective adsorption[9–11], sensing[12] and molecular ordering for generating optical functionality[13,14], is commonly based on purposefully directed exchange phenomena between the host material and the surroundings. The exchange rate, which can never be faster than allowed by the guest diffusion in the host material, is decisive for the performance of these applications[15–17].

Traditionally, guest diffusivities are measured 'macroscopically', that is, by recording the overall uptake or release induced by a step change of pressure in the surrounding atmosphere, and by predicting the internal fluxes on the basis of model assumptions[18]. With the option of recording the diffusion paths of the guest molecules over, typically, micrometres, pulsed-field-gradient NMR (PFG NMR)[16,19–22] gave rise to a critical reconsideration of this concept: the diffusion resistance of the genuine pore network was, in many cases, found to be only one among a variety of transport resistances, including barriers both on the external surface[23] and in the intracrystalline space[24]. Extrapolating molecular uptake and release as the primary attainable quantities to predict intracrystalline fluxes was thus found to lead, in many cases, to incorrect estimations of mass transfer. This result was supported by molecular dynamics simulations[25–27] and experimental evidence from both quasi-elastic neutron scattering[28–30] (monitoring mean diffusion paths over nanometres) and single-particle tracking[31–34], which were found to be in agreement with the results of NMR studies[35]. The spectrum of techniques applied for chemical imaging of nanoporous materials, notably of catalyst particles, has dramatically broadened over recent years and keeps expanding with new, promising approaches. Reference 36 provides an impressive overview of the state of the art and the main routes of further development, including the monitoring of heterogeneities within the porous solid as well as of guest distributions.

Guest monitoring by interference microscopy (IFM)[37–39] and by infrared microspectroscopy (IRM)[40–49] have proved to be applicable to a particularly large spectrum of guest molecules. They allow, in particular, the observation of transient concentration profiles with guest densities high enough so that any disturbance by insufficient statistics may be ruled out. These techniques are collectively referred to as microimaging. As a particular beauty of their application, they may deal with exactly those nanoporous host–guest systems that have already been, over decades, the focus of conventional ('macroscopic') uptake and release measurements[18,50–52], operating with but a single crystallite. By dealing with individual crystallites rather than crystallite assemblages, microimaging also allows the range over which the main parameters of mass transfer, notably intracrystalline diffusivities and surface permeabilities, may vary within a given sample to be explored. The recent application of spatiotemporal spectroscopy for the characterization of catalysts at work[36] has revealed the existence of quite impressive heterogeneities that, notably, appear when different nanoporous particles are compared.

Operating with individual crystallites does, however, also dramatically enhance the peril of corruption by spurious amounts of contamination in the sorbate supply. It was the complementarity of IFM and IRM that helped to finally overcome these limitations[47]. Over the past few years, microimaging has provided unprecedented insight into the phenomena of mass transfer in nanoporous materials, offering an impressive catalogue of data of practical utility for their optimum design and exploitation. This Progress Article illustrates some of the recent developments.

Techniques of microimaging

Figure 1 illustrates the working principles of the two microimaging techniques. The resulting profiles show, strictly speaking, concentration (c) integrals $\int_0^L c(x,y,z)\mathrm{d}z$ in the observation direction (where L is the crystal thickness) rather than the local concentrations $c(x,y,z)$. In addition to being transparent to the radiation frequency applied for observation, the nanoporous particles under study are required to be of well-defined shape, ideally with faces parallel to each other. In numerous cases (including crystals with one-dimensional channel structures, as indicated in Fig. 1b, right), mass
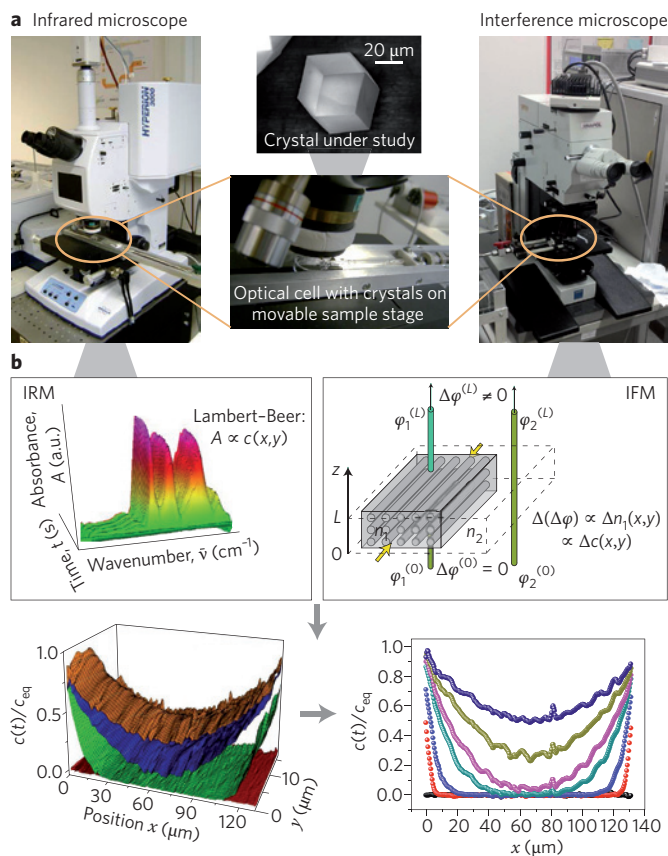
Figure 1 | Schematic of microimaging. a, The nanoporous crystal under study (centre images) is in the focus of the infrared microscope (left) or interference microscope (right), positioned within an optical cell that is connected with a vacuum system of conventional uptake and release experiments. **b**, Guest concentrations, determined by analysing the characteristic absorption bands in the infrared spectra (top left; the colours indicate the intensity of the infrared absorption bands) or the interference patterns, that is, guest-induced changes in the optical density of the crystal (top right), result as two-dimensional plots (bottom left) at subsequent times (each time is displayed in a different colour), which may be easily transferred, for example, into one-dimensional concentration (c) profiles along a particular cross section (bottom right). φ is the phase of the light beams, n the optical density and c_{eq} denotes the guest concentration in equilibrium with the gas phase. Figures reproduced with permission from: **b**, top left, ref. 53, © 2010 RSC; bottom left, ref. 90, © 2009 Wiley.

transfer in the observation direction may be excluded or neglected so that the concentration integral degenerates to the simple product $L \times c(x,y) \propto c(x,y)$. In both techniques, concentrations are determined in relative units. Absolute concentrations are determined by comparison with the adsorption isotherms $c(p)$, that is, from the guest concentrations c in equilibrium with the guest pressure p, which may be determined by either conventional gravimetric measurements or molecular modelling. Spatial resolution in IFM is given by the optical wavelength ($\sim$0.5 μm) and by the size of the pixels ($\sim$3 μm) recorded by IRM. As IRM can distinguish between different molecules by recording different absorption bands, it can also selectively record transient concentrations and fluxes in multi-component systems, including the observation of tracer-exchange phenomena. Further details may be found in refs 16,53.

With the advent of microimaging, intracrystalline guest concentrations and guest fluxes (determined from the area between subsequent concentration profiles (as shown in Fig. 1b, bottom right), divided by the time difference between their recording) became accessible by direct experimental observation. With the

Box 1 | Fundamentals of mass transfer in nanoporous materials.

The transport diffusivity D_T (Fig. B1a) is — by Fick's first law — defined as the factor of proportionality between the flux of the molecules and their concentration gradient. A related definition may be used for characterizing molecular mobility under equilibrium, that is, for uniform concentrations (Fig. B1b). It is based on a 'thought experiment' (experimentally approached using 'tracers', that is, molecules marked with two different isotopes) in which the guest molecules become distinguishable (light and dark red in Fig. B1b). Thus, once again, one may consider a factor of proportionality between the concentration gradients of either of the differently labelled molecules and their fluxes. It is referred to as the coefficient of self- or tracer diffusion D_{self}. Alternatively and completely equivalently, the self-diffusivity may also be defined by the Einstein equation $\langle x^2(t) \rangle = 2D_{self}t$ (refs 16,122) between the mean square displacement of diffusing molecules and the observation time. This relationship is the key to diffusion measurements by NMR[16,19–22] and quasi-elastic neutron scattering[28–30]. The coefficients of self- and transport diffusion do not depend on the magnitude of the chosen concentration gradients, but they do, in general, depend on the concentration. Referring to different physical situations, the coefficients of transport and self-diffusion cannot be expected to coincide. The exploration and establishment of the basic laws of their interdependence is rather an important issue of both fundamental and applied research, which we refer to in the section 'Correlating self- and transport diffusion'.

Figure B1c illustrates the situation of mass transfer through planes ('barriers') of dramatically reduced permeability. The permeability α of such barriers is defined as the factor of proportionality between the flux and the difference in concentrations on either side of the barrier. For transport resistances on the outer surface of the nanoporous particles ('surface barriers') one, correspondingly, has to consider the difference between the actual boundary concentration and the concentration in equilibrium with the gas phase.
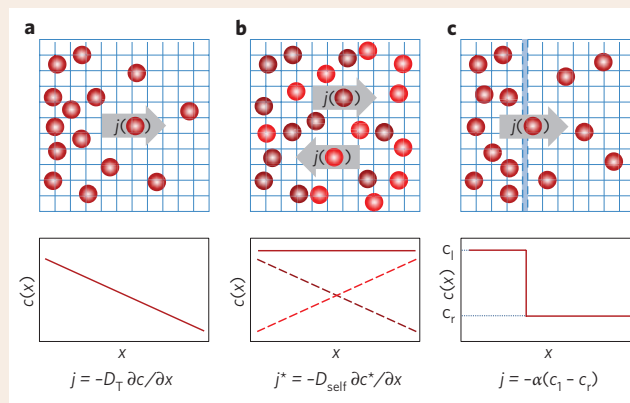

Figure B1 | Mass transfer in nanoporous materials. a–c, Molecular distribution (top), concentration (c) profiles (middle) and definition of the relevant transport parameters (bottom) during diffusion-limited uptake or release (**a**) and tracer exchange (**b**) and for mass transfer limitation by a plane of dramatically reduced permeability (**c**). D_T is the transport diffusivity, D_{self} is the coefficient of self- or tracer diffusion, α is the surface permeability, j and $j^\star$ denote the flux density of unlabelled and labelled particles, respectively, and c_l and c_r denote the concentrations on the left and right sides of the barrier.

defining equations (Fig. B1, bottom), the determination of all relevant parameters of mass transfer (Box 1) can now be based on firm experimental evidence.

Correlating self- and transport diffusion

Within the Maxwell–Stefan diffusion model[54], self- and transport diffusion can be correlated by realizing that molecules propagating under the conditions of self-diffusion (that is, during the process of counter diffusion of labelled and unlabelled molecules — see Fig. B1b) have to overcome the drag experienced by 'friction' with the host lattice and the counter-diffusing molecules. Taking the reciprocal values of the respective diffusivities as a measure of the respective resistances[16,55–57] one may thus note:

$$1/D_{self} = 1/D_{T0} + 1/\text{Đ}_{ii} \tag{1}$$

where D_{T0}, referred to as the 'corrected' diffusivity, is related to the transport diffusivity (D_T) by:

$$D_T = D_{T0} \, (\partial \ln p \, / \, \partial \ln c) \tag{2}$$

D_{self} is the coefficient of self- or tracer diffusion and Đ_{ii} is the Maxwell–Stefan self-exchange diffusivity. The reciprocal value of the logarithmic derivative of the equilibrium concentration (c) with respect to the gas pressure (p), which appears on the right-hand side of equation (2), is known as the thermodynamic factor. As c and p are proportional under the condition of ideality ($c \propto p$), in equation (2), the thermodynamic factor may thus be understood as an extra driving force for transport diffusion. It must be, correspondingly, eliminated if one is concerned with only the drag exerted by the host lattice. The reciprocal value of Đ_{ii} represents the drag experienced by the guest molecules on passing each other.

In the limit of sufficiently small concentrations (corresponding to negligible guest–guest interactions), the thermodynamic factor equals one and, moreover, any drag between the guest molecules may be neglected. Then, from equations (1) and (2), the self- and transport diffusivities are seen to coincide. This coincidence, which might already seem intuitive from Fig. B1a,b for non-interacting guest molecules, is an immediate consequence of the fact that it is only the existence of molecular interactions by which a distinction between equilibrium and non-equilibrium phenomena becomes meaningful[58].

If (in too narrow channels) the exchange in the positions of adjacent molecules is excluded (condition of single-file constraint[59–61]), the drag of self-exchange is, obviously, infinitely large and Đ_{ii} becomes, correspondingly, zero. Then, in equation (1), the self-diffusivity is also immediately seen to become zero, irrespective of the fact that the transport diffusivity may attain quite large values[62].

In the other extreme, that is, in systems where the mutual friction of counter-diffusing molecules is negligibly small compared with the drag exerted by the host system on molecular propagation, the term $1/\text{Đ}_{ii}$ on the right-hand side of equation (1) may be dropped. By combination with equation (2) we end up with:

$$D_T = D_{self} \, (\partial \ln p \, / \, \partial \ln c) \tag{3}$$

Richard Barrer[63,64] suggested this equation for correlating self- and transport diffusion decades ago. It has been shown to be strictly applicable in the absence of any cross-correlation between counter-fluxing molecules within the formalism of irreversible thermodynamics[16,56,58,65]. Owing to its similarity to an expression applied by Darken[66] for studying interdiffusion in binary metal alloys, equation (3) has become known as Darken's equation. It was, however, not before IRM made it possible to microscopically measure transport diffusion and self-diffusion under identical experimental conditions, that its extensive proof has become possible[67].

The measurements were performed using ethanol as a guest molecule and a metal–organic framework (MOF) of type ZIF-8 (zinc 2-methylimidazolate)[68] as a host system (Fig. 2), with great potential for pervaporation processes[69]. ZIF-8 accommodates cages connected by narrow 'windows' of molecular dimensions. Guest diffusion is thus controlled by the passage through the windows. Such passages may be considered as 'rare events' so that the probability of molecular encounters within these windows is negligibly small and guest diffusion remains essentially unaffected by mutual 'friction' of the guest molecules. Equation (3) may therefore be expected to be strictly applicable.

The data on D_T and D_{self} for ethanol (Fig. 2) demonstrate the coincidence between the experimentally determined
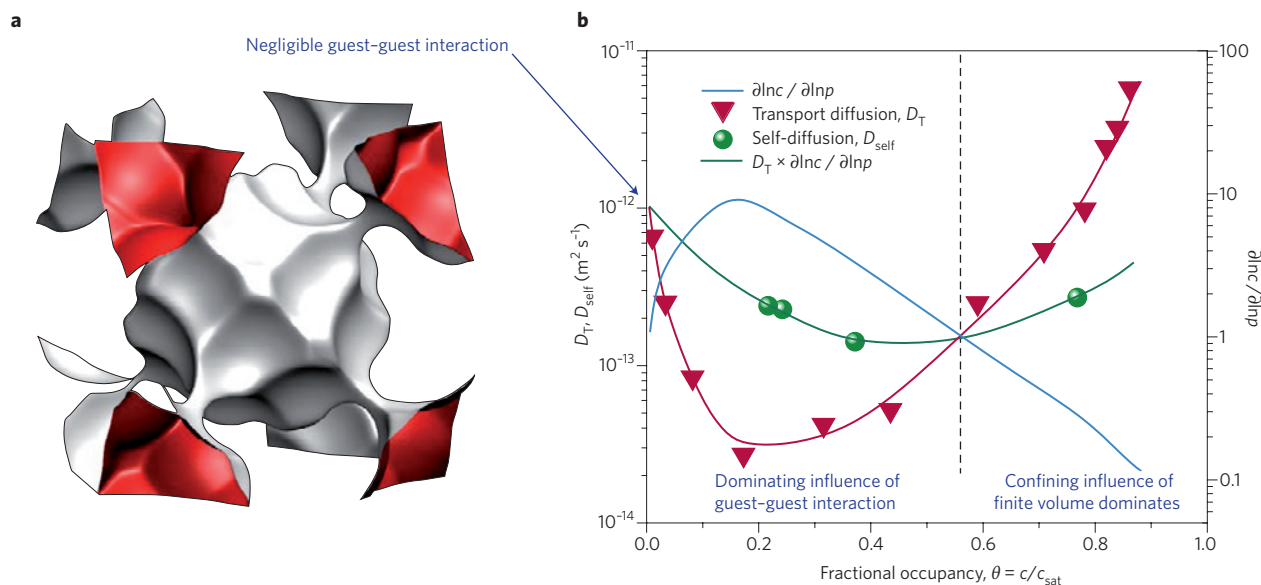

Figure 2 | Correlation of self- and transport diffusion. a, 'Landscape' of the potential energy experienced by a guest molecule in ZIF-8. Shown is one ZIF-8 cage with the 'windows' connecting it with its eight neighbouring cages. **b**, The experimentally determined coefficients of self- (D_{self}) and transport (D_T) diffusion of ethanol at room temperature (data points), together with the self-diffusivities (green line) predicted via equation (3) from the fit of the measured transport diffusivities (red line) and the adsorption isotherm. c is concentration, c_{sat} is the saturation concentration and p is pressure. The black dashed line separates the occupancy regions where the guest–guest interaction or the confinement by the finite pore volume dominate the mass transfer. For the original data see refs 53,67.

self-diffusivities (green data points) and their predicted values (green line) from D_T data using equation (3). From equation (3), the merging of the self- and transport diffusivities (intuitively anticipated from the representations in Fig. B1) is seen to be caused by the system's ideality at low concentrations, implying proportionality between pressure and concentration.

Figure B1 is also helpful for intuitively rationalizing the inversion in the relationship between the self- and transport diffusivities on passing from small to high concentrations. In transport diffusion, with increasing concentrations, the increasing interaction between the (polar) guest molecules will progressively counteract the 'driving force' of the concentration gradient and reduce the flux to regions of lower concentration, compared with self-diffusion. With further increasing concentration, however, the effect of steric confinement makes the molecules 'more willingly' propagate to regions of lower concentration, leading to flux enhancement, compared with self-diffusion.

The results of these studies were nicely supported by complementary measurements exploiting methanol and ethane as guest molecules[67]. For methanol, as a more polar guest molecule, the range of dominating guest–guest interactions (giving rise to $\partial \ln c / \partial \ln p > 1$ and, hence, to reduced transport diffusivities, Fig. 2b, left) is found to be notably extended, close to saturation. The reverse is true for the apolar and bulkier guest ethane. Here, again starting

from essentially coinciding values at small loadings, the transport diffusivities are found to exceed the self-diffusivities progressively with increasing loading.

Surface permeabilities and sticking probabilities

In situations where intercrystalline molecular exchange occurs at rates far below the values estimated from the intracrystalline diffusivities, PFG NMR proved to serve as a valuable tool for the detection of surface barriers[23,70–72]. The accurate determination of their permeability, however, has only become possible with the advent of microimaging.

An example illustrating significant differences in permeabilities across different crystal faces is provided by zeolites of type SAPO STA-7[73,74]. Figure 3 shows their pore structure and crystal composition (a), crystal shape (b) and snapshots during the process of crystal fracturing (b–e), which occurs during their activation (that is, evacuation at increased temperatures) before the uptake experiments[73]. Fracturing is known to occur with SAPO STA-7 crystals of high silicon content (Si/(Si + P) = 0.37 in the chosen example). The atomic force microscopy image of the surface of the (still intact) crystal before activation (f) exhibits a 'fault line' (framed by the dotted lines), which may be taken as an indication of the origin of the emerging new face.

Figure 3g illustrates the dramatic enhancement of the permeability of the freshly formed surface plane compared with the
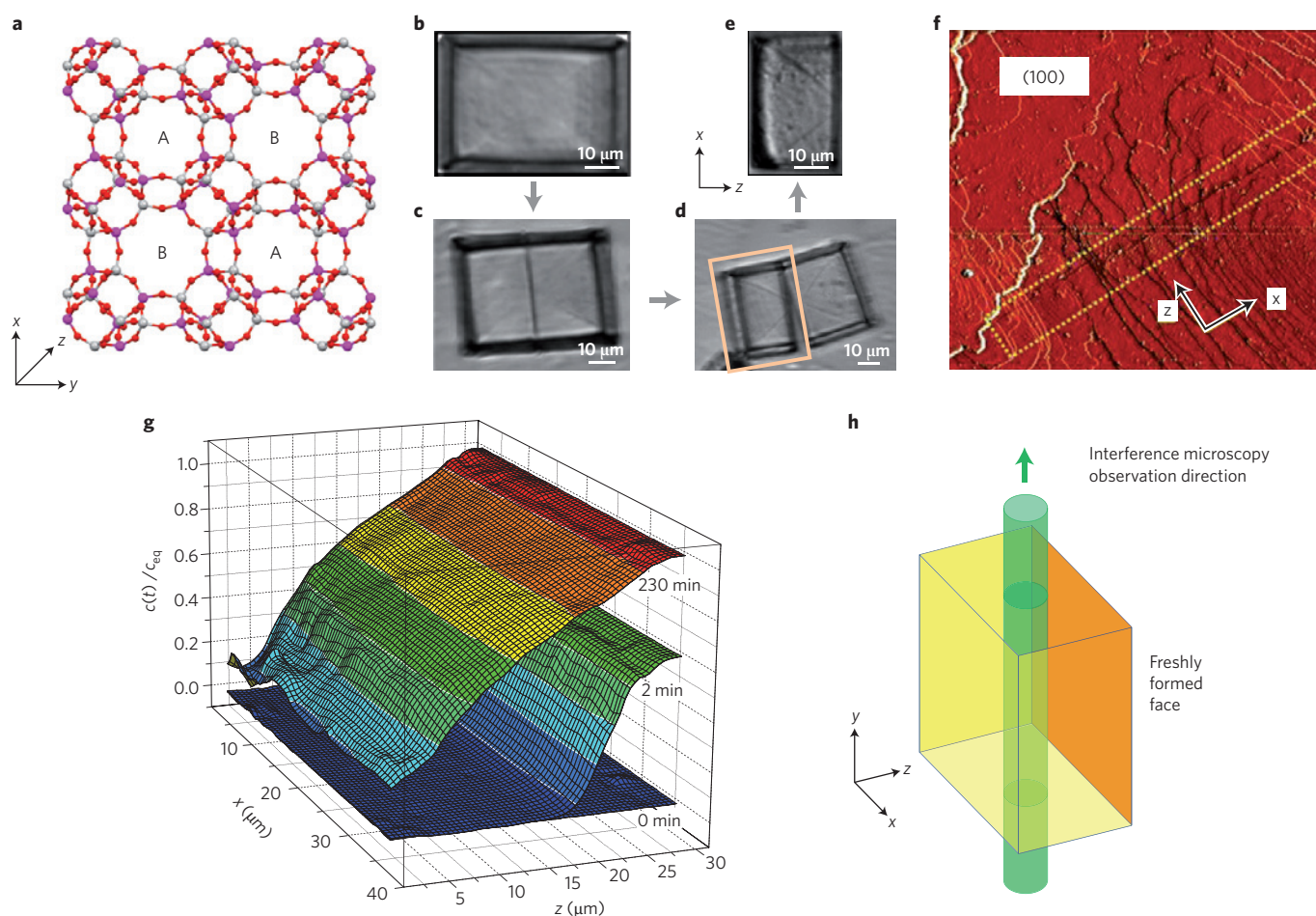

Figure 3 | Non-uniform surface of zeolite SAPO STA-7. a, Pore structure. Fourfold-connected grey and purple balls represent aluminium, phosphorus or silicon; the red balls in between represent the connecting oxygen atoms. **b–e**, Optical images of an SAPO STA-7 crystal showing crystal fracturing during activation. The detached crystal fragment in **e** is framed by the orange box in **d**. **f**, Atomic force microscopy image of the crystal surface before activation. The dotted lines frame a fault line. **g,h**, Transient guest profiles at room temperature during methanol uptake by a pressure step from 0 to 0.1 kPa (**g**) after splitting, observed with the crystal orientation schematically shown in **h**; the novel (fractured) crystal face is indicated by darker shading. *c* denotes concentrations and c_{eq} denotes the guest concentration in equilibrium with the gas phase. Figure reproduced with permission from ref. 75, © 2010 ACS.

permeability through the 'old' crystal faces in the {001} direction. Using methanol as a probe molecule, two minutes after the onset of adsorption, the guest concentration close to the freshly formed face is seen to have attained more than half of its equilibrium value while, after as long as four hours, the boundary concentration close to the 'old' face still amounts to not more than 20%. Possible reasons for explaining this dramatic difference include the existence of composition variation in the {001} direction, just as ageing effects on the crystal surface revealing structural lability to be much more pronounced close to the crystal surface than in the crystal bulk phase[75].

Already in the early NMR studies[70], the formation of surface resistances in LTA-type zeolites on technological use for mass separation was correlated with lattice collapse close to the crystal surface[71] and coke depositions[23,72]. Only now, however, with the precision of microimaging, permeabilities of surface barriers may be determined with accuracies that allow a more profound analysis of their origin. On comparing different crystallites of one and the same nanoporous material specimen, the variation of the intracrystalline diffusivities was found to be notably exceeded by the variation of the surface permeability, as another indication of structural instability and, hence, variability, close to the surface. It came, however as a real surprise when in extensive IFM studies of the transient sorption of light paraffins with MOFs of type Zn(tbip) (tbip = tert-butyl isophthalate)[76] the dependences of the intracrystalline transport diffusivities, D_T, and surface permeabilities, α, on guest loading and temperature were found to essentially coincide[77]. Moreover, for a given crystal, the ratio of α and D_T is found to be nearly independent of the guest species[78]. Surface permeation and intracrystalline diffusion were thus seen to proceed by identical elementary mechanisms. These barriers cannot be formed, therefore, by an essentially homogenous layer of dramatically reduced permeability. We have rather to imply that there are only a few connections ('windows') between the intracrystalline pore space and
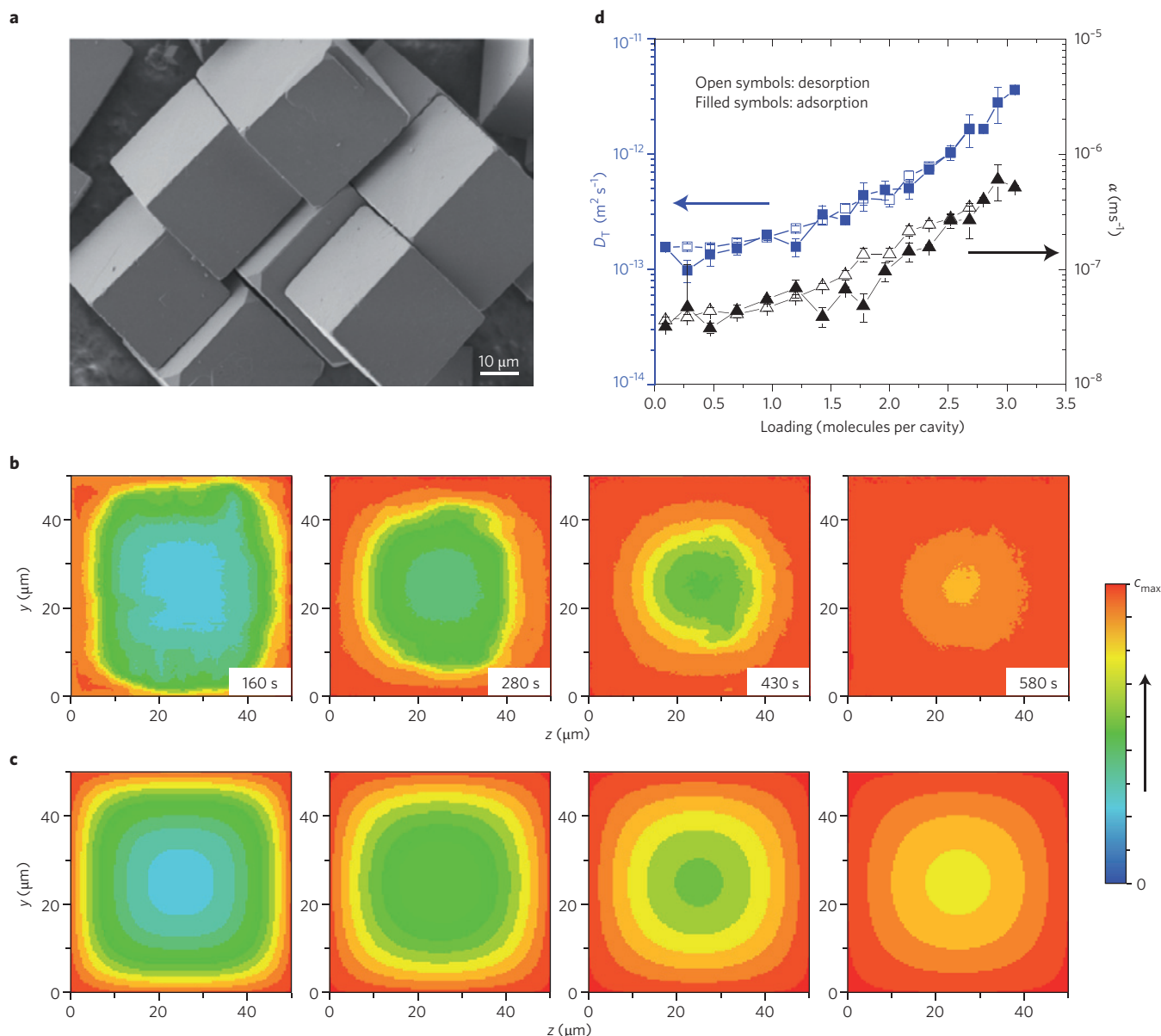
Figure 4 | Unravelling the nature of surface barriers. a, Scanning electron microscope image of the crystals of zeolite AlPO-LTA. **b**, Transient concentration profiles at room temperature during propene uptake by a pressure step from 0 to 25 kPa recorded by interference microscopy. **c**, Comparison with the analytical solution. c_{max} is the maximum concentration. **d**, The resulting intracrystalline transport diffusivities, D_T, and surface permeabilities, α, as a function of loading. Figure reproduced with permission from ref. 81, © 2012 ACS.

the surrounding atmosphere while the remaining part of the surface is totally impermeable[79,80].

The diffusivity data for propene in AlPO-LTA[81], a cation-free representative of the zeolite LTA family[82–84], (Fig. 4) demonstrate that the correlation between D_T and α is also a characteristic of other guest–host combinations. This provides a rationalization of the experimental observations that the microscopically determined intracrystalline diffusivities do often exceed the 'macroscopic' diffusivities by orders of magnitude, while their dependences on, for example, loading, temperature, cation content and molecular size coincide[16,85,86].

From the effective medium theory[87], the permeability through an impermeable boundary with circular holes of diameter d and separation L is known to obey the relationship $\alpha = D \times d/L^2$. On the basis of this relationship, with the experimental diffusivity and permeability data of ref. 81, only one out of several thousands of such openings connecting the intracrystalline space of the AlPO-LTA sample under study with the surroundings is found to be permeable for propene.

The existence of surface barriers and the option of their quantitation by microimaging enables the application of the concept of sticking probabilities to nanoporous materials. In heterogeneous catalysis, it denotes the probability that, on colliding with a catalyst surface, a molecule will not return into the surrounding atmosphere[88]. With nanoporous materials it would, correspondingly, stand for the probability that, after encountering the outer surface of a nanoporous particle, a molecule will enter the internal pore space. The sticking probability is of similar relevance, as it is the internal pore space where the molecules are subject to the (steric) conditions that have been selected for achieving the technologically desired separation and conversion phenomena.

As the flux of molecules colliding with a surface can be estimated using the kinetic theory of gases[89], it remains to determine the flux of molecules passing the surface barrier. The flux through the surface as determined by microimaging is the difference between the counter-directed fluxes leaving and entering the crystal. Under equilibrium conditions, the influx is balanced by the efflux of molecules, given by $\alpha \times c_{eq}$, where c_{eq} denotes the guest concentration in equilibrium with the gas phase. Like their 'classical' counterparts[88], sticking coefficients on nanoporous materials are observed to attain quite different values, depending on the system under study.

For propane in MOF Zn(tbip), for example, sticking probabilities of as low as 5×10^{-8} have been observed[90]. This means that, out of about 20 million propane molecules colliding with the surface of a crystal of MOF Zn(tbip), only a single one enters the intracrystalline pore space while all others (namely 20 million) are expelled. Together with the surface permeabilities, the sticking probabilities may be significantly affected by the influence of structural variations induced by the given procedure of sample storage, pretreatment and/or application. With MFI-type zeolites, for example, the sticking probability of isobutane was observed to drop from values >0.01 to <10^{-4} by subsequent adsorption–desorption cycles[91]. These changes were attributed to the influence of spurious amounts of water, which were found to leave the intracrystalline diffusivities essentially unaffected and exclusively affect the external surface of the given nanoporous crystal[92]. In complete agreement with this concept, permeabilities and, hence, sticking probabilities are in general observed to be significantly larger on freshly cut crystal faces than on 'older' ones[75,93], while the intracrystalline diffusivities remain essentially unchanged.

Anisotropy and mixture diffusion effects

By microscopically recording guest fluxes within a given host crystal, microimaging offers the most direct access to tracing diffusion anisotropy in crystals. Diffusion anisotropy, that is, orientation-dependent propagation rates, are the key to molecular traffic control[94]

wherein differences in the diffusion pathways of the reactant and product molecules[95,96] are exploited to enhance reactivity.

FER[97–100], an industrially important crystalline zeolite of non-cubic symmetry, was in the focus of the very first extensive IFM investigations of transient concentration profiles[101]. FER crystals have orthorhombic symmetry and are traversed by two sets of parallel channels in the crystallographic y and z directions (Fig. 5a).

From the transient concentration profiles, the openings of the larger (ten-ring) channels were determined as being essentially blocked, so that uptake and release of guest molecules occurred predominantly via the smaller (eight-ring) channels. This finding led to the development of a special sample treatment, involving washing with NaOH solution, that removes these blockages[100]. The evolution of the guest profiles (shown in Fig. 5b for methanol and in Fig. 5c for ethanol) in the thus pre-treated specimens of FER do reflect the expected behaviours, namely uptake occurring essentially exclusively along the wider ten-ring channels in the z direction, accompanied by a negligibly small uptake along the eight-ring channels. Sample treatment did, once again, lead to dramatic changes in the surface permeabilities and, hence, the sticking probabilities, with the intracrystalline diffusivities remaining essentially unchanged. It is interesting to note, however, that only with these modifications did some features of intracrystalline mass transfer (namely the diffusivities in channel direction) become accessible by direct measurement. Quantitative analysis of the propagation rate of the diffusion fronts at low concentrations yields, for the ten-ring channels, diffusivities ($D_z \approx 2 \times 10^{-10}$ m² s⁻¹ for methanol and $D_z \approx 8 \times 10^{-15}$ m² s⁻¹ for ethanol) that exceed those in the eight-ring channels ($D_y \approx 2 \times 10^{-13}$ m² s⁻¹ for methanol and $D_y \approx 1 \times 10^{-16}$ m² s⁻¹ for ethanol) by several orders of magnitude[102,103]. The dramatic decrease of the diffusivities in the smaller channels corresponds to the fact that the critical guest diameters (0.375 nm for methanol and 0.47 nm for ethanol) are comparable to the channel diameters. Further decreases in channel diameters will result in dramatic reductions in molecular mobilities.

In Fig. 5a, the FER crystals are shown to exhibit roof-like segments on their upper and lower faces. As microimaging records the integral over the concentrations rather than the concentrations themselves, the existence of these segments must, in principle, be taken into account on translating the measured concentration integrals into local concentrations[103]. However, as long as the uptake by the roof-like segments is negligibly small compared with the uptake by the side faces, there is no need for such a correction. This is, essentially, the situation during the initial stages of molecular uptake considered in Fig. 5b–d.

In separation technologies, nanoporous materials are invariably in contact with mixtures of guest species rather than with only a single component. The proper understanding and modelling of diffusion is additionally complicated as the mobility of one species is also affected by the other component(s)[56]. Particularly complex effects of mutual hindering are known to occur in mixtures of alcohol and water[104], a system of industrial relevance for pervaporation separations based on nanoporous membranes[105].

The large differences in the unary diffusivities of methanol and ethanol in FER, apparent from Fig. 5b,c, may be exploited for attaining hitherto inaccessible information about their interplay in mixtures. For this purpose, a two-step experiment was performed. As a first step, an activated FER crystal was subject to an atmosphere of ethanol, repeating exactly the situation shown already in Fig. 5c. After 1.8 h, the ethanol atmosphere was replaced by a methanol atmosphere. The transient concentration profiles during the subsequent methanol uptake are shown in Fig. 5d.

Comparison of Fig. 5d and b reveals a striking difference. Deviating from its unary behaviour, methanol uptake in the mixture is now seen to occur predominantly perpendicular to the crystal's longitudinal extension, that is, in the eight-ring rather than
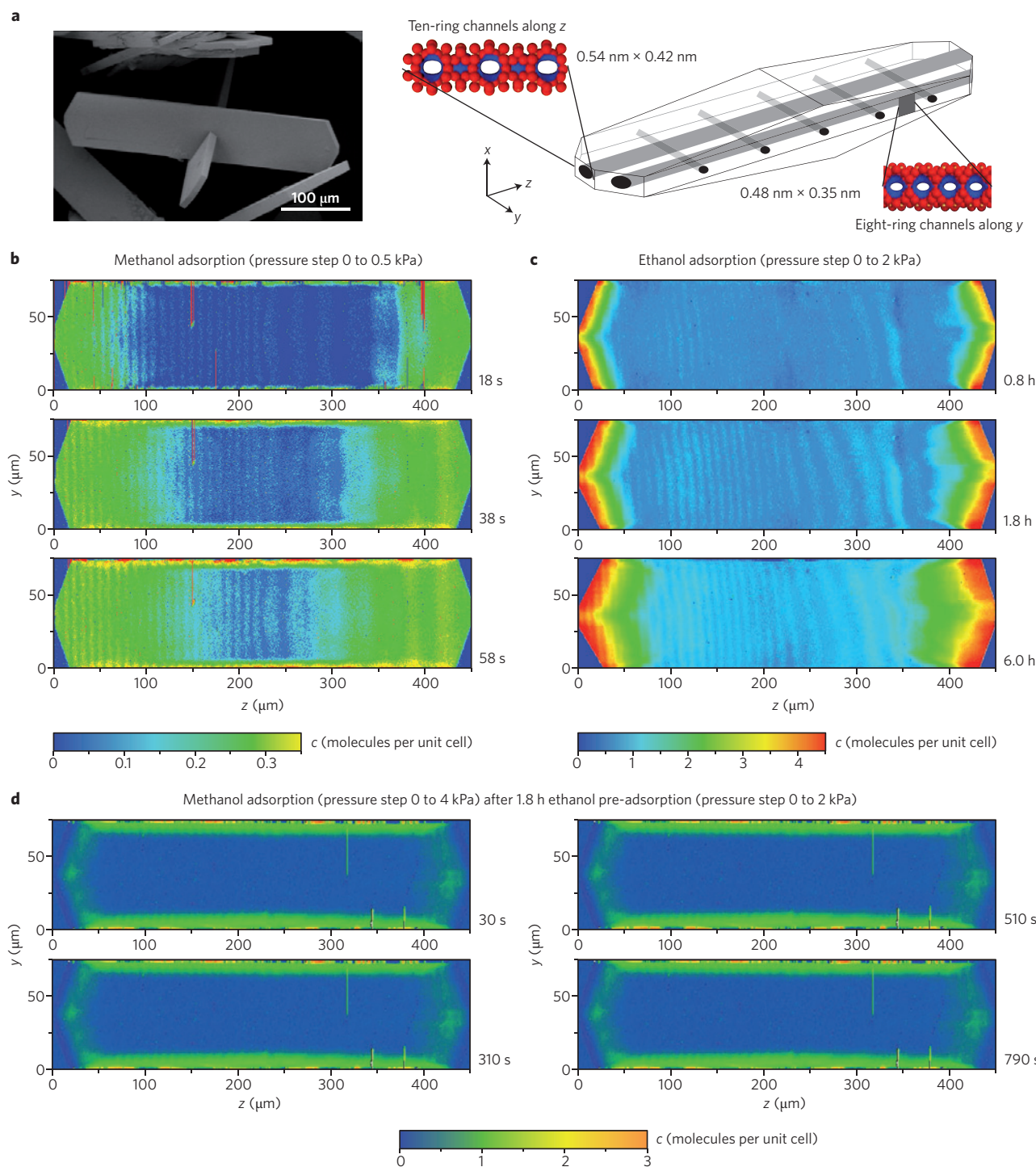
Figure 5 | Diffusion anisotropy and mixture diffusion effects in FER-type zeolites. a, Reflection electron microscopy image (left) and schematic (right) of a zeolite crystal of type FER accommodating two sets of nanoporous channels. **b–d**, Transient guest profiles during methanol (**b**) and ethanol (**c**) uptake, as well as during methanol uptake (**d**) as the second step in a two-step experiment, preceded by ethanol uptake over 1.8 h. In Fig. 5d use has been made of the fact that the ethanol mobilities are negligibly small compared with methanol. Hence, variations in the refractive index may be considered to be caused by changes in the methanol composition. Figures reproduced with permission from: **a**, left, ref. 100, © 2011 ACS; **b**, ref. 102, © 2011 AIP.

ten-ring direction. For rationalizing the origin of this reversal in the diffusion pathways, we consider the changes in the transport resistances experienced by the methanol molecules after ethanol pre-adsorption. Before propagating into the interior of the FER crystals, the methanol molecules have to permeate a layer where they have to pass the notably larger ethanol molecules. The layer, therefore, has the characteristics of a surface barrier. From the

ethanol distributions shown in Fig. 5c, its extension in the z direction is seen to amount to some tens of micrometres, whereas it is still beyond the limit of resolution in the y direction. The reversal in the preferred diffusion pathways after ethanol pre-sorption can thus be correlated with the fact that, during the foregoing step of ethanol adsorption, the amount of ethanol molecules entering the ten-ring channels dramatically exceeds those in the eight-ring

channels. The transport resistance additionally experienced by the methanol molecules due to the presence of the ethanol molecules may thus indeed be expected to remain quite small within the eight-ring channels, whereas it leads to a dramatic retardation of transport in the ten-ring channel. In fact, this retardation is seen to be so powerful that now diffusion along the (smaller) eight-ring channels becomes the governing mechanism of methanol uptake.

Guest-induced phase transitions

There is, at present, a great deal of attention in the published literature on guest-induced structural changes in crystalline materials.

Phenomena such as gate opening[106] and breathing[107–109] can be exploited to achieve enhanced separation performance. An industrially important example is that of separation of aromatic mixtures containing benzene and xylenes, using MFI zeolite. Starting with concentrations of about four molecules per unit cell, changes in the lattice structure could be unambiguously recorded by both X-ray diffraction analysis[110,111] and high-resolution solid-state NMR spectroscopy[111,112]. These findings were reproduced in simulations with flexible zeolite lattices considering the influence of the guest molecules[113,114]. These systems invariably exhibit strong isotherm inflections[115,116], accompanied by a steep increase in diffusivity[57].

c MFI-type channel system
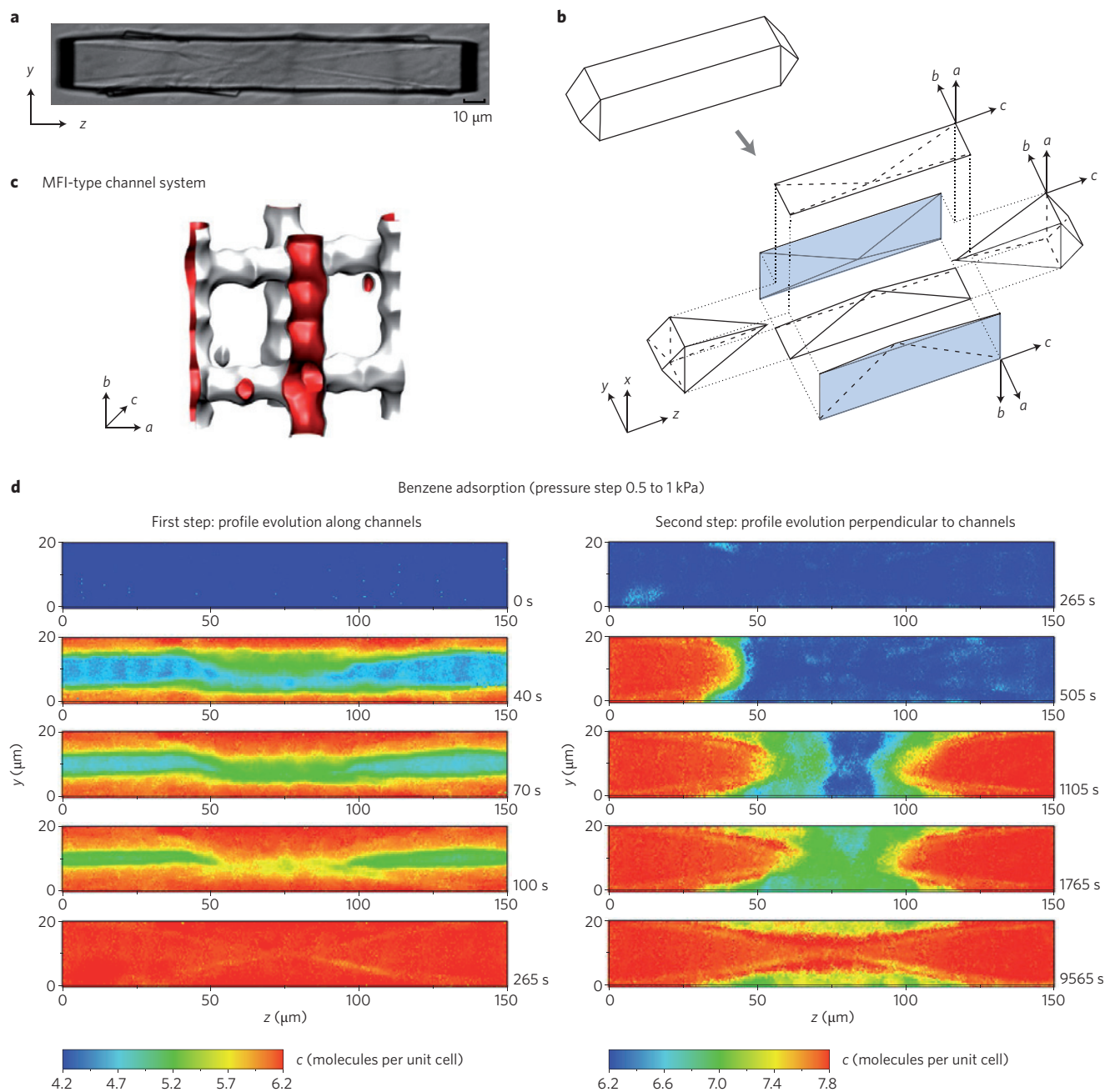
d

Benzene adsorption (pressure step 0.5 to 1 kPa)

Figure 6 | Imaging of a guest-induced phase transition in MFI-type zeolite. a, Optical image of MFI-type crystallite. **b,c**, Schematic representation and arrangement of the building blocks generally assumed to constitute 'coffin-shaped' MFI-type crystallites (**b**), with a view into their pore system (**c**), exhibiting 'straight' channels in the crystallographic *b* direction and 'sinusoidal' channels in the *a* direction. **d**, The variation of the refractive index after benzene adsorption, induced by a pressure step from 0.5 to 1 kPa, is represented in terms of local concentrations averaged in the observation direction (that is, perpendicular to one large side face, where the four possible observation directions yielded essentially identical patterns). The overall process is seen to consist of two steps (left and right columns), with significantly differing time constants. Both steps are presented in the same colour code, with the initial stages in blue and the final ('equilibrium') ones in red. Panel **c** reproduced with permission from ref. 56, © 2012 RSC.

Such transitions can be shown to be associated with a re-distribution of the molecules[116], resulting in their shift from the pore channel intersections as their preferred locations at low loadings (being, at half loading, completely occupied) into the channel interiors. Correlating guest concentrations and locations with host-framework structural changes is further complicated by the large number of possible crystal morphologies, ranging to 18, for MFI[117].

The exploration of benzene uptake in MFI-type zeolites by microimaging (Fig. 6) leads to surprising findings. After an initial period of normal uptake (characterized by guest profiles evolving along the channel system in the y direction, that is, perpendicular to the longitudinal extension of the crystal, Fig. 6d, left), concentration profiles evolve (Fig. 6d, right) in the crystal's longitudinal (z) extension. The two channel systems in MFI-type zeolites (Fig. 6a–c), however, are extended in x and y directions only, leading to dramatically reduced diffusivities in the z direction[118]. The propagation of the concentration front can thus not be referred anymore to mass transfer. It must rather be considered as an indication of long-term phase changes in the host–guest system, which, accordingly, also gives rise to changes in the corresponding equilibrium concentrations of the guest molecules.

Note that the 'concentrations' plotted in Fig. 6d are determined on the basis of the (guest-induced) changes in the refractive index (representing the primary data of microimaging by interference microscopy). The phase transition in the host–guest system, observed with the second step in molecular uptake, must be expected to be accompanied by changes in orientations and rotational freedom of the guest molecules, which can also be expected to give, for selected crystal orientations, rise to changes in the polarizability and, hence, in refractive index and optical density. This is obviously true with the extended triangles on the upper and lower crystal faces so that, in the right column of Fig. 6d, the colour code does not apply anymore to these regions. Even with continued observation after the last profile shown in Fig. 6d over the same time interval again (namely in total up to 23,000 s ≈ 6.4 h), no further changes became visible. The system is thus seen to have finally attained equilibration. In fact, the difference in the optical densities between different crystal regions, which has emerged and continues to remain under equilibrium, may thus be taken as a further confirmation of the phase transition within the host–guest system whose spatial evolution inside the crystals has now become accessible by direct observation.

Conclusions and outlook

Nanoporous materials do occur in an excitingly broad variety, essentially unlimitedly growing by the power of novel synthesis concepts[8,119–121]. The advent of microimaging techniques has provided us with a tool by which, for the first time, guest profiles within these materials can directly be monitored. Observing the variation in these profiles affords unprecedented insight into transport phenomena, including intracrystalline diffusion and surface permeation. None of these results have been accessible before and attaining some of them might even have been unimaginable.

The novel information obtained using microimaging concerns the hot topics of current material-related fundamental research, with the interrelation between the 'different' diffusivities and their correlation with surface permeabilities being prominent examples. Simultaneously, it concerns issues of immediate relevance for the technological performance of these materials, as mass transfer is among the key phenomena controlling the output of value-added products by such materials. Microimaging-controlled removal — just as, vice versa, the purposeful creation — of surface barriers might thus become one of the appealing new challenges in fabricating nanoporous materials with transport properties optimized for any specific application.

In particular, under the conditions of multicomponent adsorption, new types of insight were obtained. Commonly, adsorption and diffusion do not proceed hand-in-hand and stronger adsorption implies lower mobility[57]. Microimaging of methanol and ethanol mixture transport within the channels of FER was shown to reveal an uncommon synergy between adsorption and diffusion, resulting in a reversal in the preferred diffusion pathways of methanol if preceded by ethanol adsorption. A reversal in the direction of guest propagation was also observed with benzene in MFI, this time induced by a phase transition in the host–guest system. Both phenomena could potentially be exploited in mass separation. Thus, in addition to the unprecedented reliability and accuracy of the data on mass transfer thus accessible, the benefit of microimaging in materials science and technology is seen to also include the exploration of so far hidden transport phenomena, with the option of their exploitation in new technologies.

References

1. Ruthven, D. M., Farooq, S. & Knaebel, K. S. *Pressure Swing Adsorption* (VCH, 1994).
2. Schüth, F., Sing, K. S. W. & Weitkamp, J. (eds.) *Handbook of Porous Solids* (Wiley-VCH, 2002).
3. Bloch, E. D. *et al.* Hydrocarbon separations in a metal-organic framework with open iron(II) coordination sites. *Science* **335,** 1606–1610 (2012).
4. Herm, Z. R. *et al.* Separation of hexane isomers in a metal-organic framework with triangular channels. *Science* **340,** 960–964 (2013).
5. Nugent, P. *et al.* Porous materials with optimal adsorption thermodynamics and kinetics for CO₂ separation. *Nature* **495,** 80–84 (2013).
6. Ertl, G., Knözinger, H., Schüth, F. & Weitkamp, J. (eds.) *Handbook of Heterogeneous Catalysis* 2nd edn (Wiley-VCH, 2008).
7. Corma, A., Nemeth, L. T., Renz, M. & Valencia, S. Sn-zeolite beta as a heterogeneous chemoselective catalyst for Baeyer–Villiger oxidations. *Nature* **412,** 423–425 (2001).
8. Perez-Ramirez, J. Zeolite nanosystems: imagination has no limits. *Nature Chem.* **4,** 250–251 (2012).
9. Kuznicki, S. M. *et al.* A titanosilicate molecular sieve with adjustable pores for size-selective adsorption of molecules. *Nature* **412,** 720–724 (2001).
10. Shimomura, S. *et al.* Selective sorption of oxygen and nitric oxide by an electron-donating flexible porous coordination polymer. *Nature Chem.* **2,** 633–637 (2010).
11. Li, J-R. *et al.* Porous materials with pre-designed single-molecule traps for CO₂ selective adsorption. *Nature Commun.* **4,** 1538 (2013).
12. Yanai, N. *et al.* Gas detection by structural variations of fluorescent guest molecules in a flexible porous coordination polymer. *Nature Mater.* **10,** 787–793 (2011).
13. Davis, M. E. Ordered porous materials for emerging applications. *Nature* **417,** 813–821 (2002).
14. Sato, H., Matsuda, R., Sugimoto, K., Takata, M. & Kitagawa, S. Photoactivation of a nanoporous crystal for on-demand guest trapping and conversion. *Nature Mater.* **9,** 661–666 (2010).
15. Laeri, F., Schüth, F., Simon, U. & Wark, M. (eds.) *Host-Guest-Systems Based on Nanoporous Crystals* (Wiley-VCH, 2003).
16. Kärger, J., Ruthven, D. M. & Theodorou, D. N. *Diffusion in Nanoporous Materials* (Wiley-VCH, 2012).
17. Tsotsalas, M. *et al.* Impact of molecular clustering inside nanopores on desorption processes. *J. Am. Chem. Soc.* **135,** 4608–4611 (2013).
18. Ruthven, D. M., Brandani, S. & Eic, M. in *Adsorption and Diffusion* (eds Karge, H. G. & Weitkamp, J.) 45–85 (Springer, 2008).
19. Kärger, J. & Caro, J. Interpretation and correlation of zeolitic diffusivities obtained from nuclear magnetic resonance and sorption experiments. *J. Chem. Soc. Faraday Trans. I* **73,** 1363–1376 (1977).
20. Valiullin, R. *et al.* Exploration of molecular dynamics during transient sorption of fluids in mesoporous materials. *Nature* **430,** 965–968 (2006).
21. Price, W. S. *NMR Studies of Translational Motion* (Cambridge Univ. Press, 2009).
22. Kimmich, R. *Principles of Soft-Matter Dynamics* (Springer, 2012).
23. Kärger, J. *et al.* NMR study of mass transfer in granulated molecular sieves. *AIChE J.* **34,** 1185–1189 (1988).
24. Vasenkov, S. *et al.* PFG NMR study of diffusion in MFI-type zeolites: evidence of the existence of intracrystalline transport barriers. *J. Phys. Chem. B* **105,** 5922–5927 (2001).
25. Yashonath, S., Demontis, P. & Klein, M. L. A molecular-dynamics study of methane in zeolite NaY. *Chem. Phys. Lett.* **153,** 551–556 (1988).
26. Theodorou, D. N., Snurr, R. Q. & Bell, A. T. in *Comprehensive Supramolecular Chemistry* (eds Alberti, G. & Bein, T.) 507–548 (Pergamon, 1996).

27. Keil, F. J., Krishna, R. & Coppens, M. O. Modeling of diffusion in zeolites. *Rev. Chem. Eng.* **16,** 71–197 (2000).

28. Jobic, H., Bee, M., Caro, J., Bülow, M. & Kärger, J. Molecular self-diffusion of methane in zeolite ZSM-5 by quasi-elastic neutron-scattering and nuclear magnetic-resonance pulsed field gradient technique. *J. Chem. Soc. Faraday Trans. I* **85,** 4201–4209 (1989).

29. Jobic, H. in *Catalyst Characterization: Physical Techniques for Solid Materials* (ed. Imelik, B. V. J. C.) 347–376 (Plenum, 1994).

30. Jobic, H., Kärger, J. & Bee, M. Simultaneous measurement of self- and transport diffusivities in zeolites. *Phys. Rev. Lett.* **82,** 4260–4263 (1999).

31. Kirstein, J. *et al.* Exploration of nanostructured channel systems with single-molecule probes. *Nature Mater.* **6,** 303–310 (2007).

32. Zürner, A., Kirstein, J., Döblingern, M., Bräuchle, C. & Bein, T. Visualizing single-molecule diffusion in mesoporous materials. *Nature* **450,** 705–709 (2007).

33. Weckhuysen, B. M. Chemical imaging of spatial heterogeneities in catalytic solids at different length and time scales. *Angew. Chem. Int. Ed.* **48,** 4910–4943 (2009).

34. Weckhuysen, B. M. (ed.) *In-situ* characterization of heterogeneous catalysts. *Chem. Soc. Rev.* **39,** 4541–5072 (2010).

35. Feil, F. *et al.* Single-particle and ensemble diffusivities — test of ergodicity. *Angew. Chem. Int. Ed.* **51,** 1152–1155 (2012).

36. Buurmans, I. L. C. & Weckhuysen, B. M. Heterogeneities of individual catalyst particles in space and time as monitored by spectroscopy. *Nature Chem.* **4,** 873–886 (2012).

37. Schemmert, U., Kärger, J. & Weitkamp, J. Interference microscopy as a technique for directly measuring intracrystalline transport diffusion in zeolites. *Micropor. Mesopor. Mater.* **32,** 101–110 (1999).

38. Geier, O. *et al.* Interference microscopy investigation of the influence of regular intergrowth effects in MFI-type zeolites on molecular uptake. *J. Phys. Chem. B* **105,** 10217–10222 (2001).

39. Lehmann, E. *et al.* Inhomogeneous distribution of water adsorbed under low pressure in CrAPO-5 and SAPO-5: an interference microscopy study. *J. Phys. Chem. B* **107,** 4685–4687 (2003).

40. Schüth, F. Polarized Fourier transform infrared microscopy as a tool for structural analysis of adsorbates in molecular sieves. *J. Phys. Chem.* **96,** 7493–7496 (1992).

41. Schüth, F. & Althoff, R. Analysis of active-site distribution in ZSM-5 crystals by infrared microscopy. *J. Catal.* **143,** 338–394 (1993).

42. Müller, G., Narbeshuber, T. F., Mirth, G. & Lercher, J. A. IR microscopic study of sorption and diffusion of toluene in ZSM5. *J. Phys. Chem. B* **98,** 7436–7439 (1994).

43. Schüth, F., Demuth, D. & Kallus, S. in *Studies in Surface Science and Catalysis, Vol. 84. Zeolites and Related Microporous Materials: State of the Art 1994 — Proc. 10th Int. Zeolite Conference* (eds Weitkamp, J., Karge, H. G., Pfeifer, H. & Hölderich, W.) 1223–1229 (Elsevier, 1994).

44. Hermann, M., Niessen, W. & Karge, H. G. in *Catalysis by Microporous Materials* (eds Beyer, H. K., Karge, H. G., Kiricsi, I. & Nagy, J. B.) 131–138 (Elsevier, 1995).

45. Lehmann, E. *et al.* Regular intergrowth in the AFI type crystals: influence on the intracrystalline adsorbate distribution as observed by interference and FTIR-microscopy. *J. Am. Chem. Soc.* **124,** 8690–8692 (2002).

46. Chmelik, C. *FTIR Microscopy as a Tool for Studying Molecular Transport in Zeolites* PhD thesis, Univ. Leipzig (2007).

47. Karge, H. G. & Kärger, J. in *Adsorption and Diffusion* (eds Karge, H. G. & Weitkamp, J.) 135–206 (Springer, 2008).

48. Stavitski, E. *et al. In situ* synchrotron-based IR microspectroscopy to study catalytic reactions in zeolite crystals. *Angew. Chem. Int. Ed.* **47,** 3543–3547 (2008).

49. Stavitski, E. & Weckhuysen, B. M. Infrared and Raman imaging of heterogeneous catalysts. *Chem. Soc. Rev.* **39,** 4615–4625 (2010).

50. Barrer, R. M. Intracrystalline diffusion. *Adv. Chem. Ser.* **102,** 1–9 (1971).

51. Barrer, R. M. & Clarke, D. J. J. Diffusion of some n-paraffins in zeolite A. *Chem. Soc. Faraday Trans. I* **70,** 535–548 (1974).

52. Ruthven, D. M. *Principles of Adsorption and Adsorption Processes* (Wiley, 1984).

53. Chmelik, C. & Kärger, J. *In-situ* study on molecular diffusion phenomena in nanoporous catalytic solids. *Chem. Soc. Rev.* **39,** 4864–4884 (2010).

54. Krishna, R. & Wesselingh, J. A. *Chem. Eng. Sci.* **45,** 1779–1791 (1990).

55. Krishna, R. Describing the diffusion of guest molecules inside porous structures. *J. Phys. Chem. C* **113,** 19756–19781 (2009).

56. Krishna, R. Diffusion in porous crystalline materials. *Chem. Soc. Rev.* **41,** 3099–3118 (2012).

57. Krishna, R. & van Baten, J. M. Influence of adsorption thermodynamics on guest diffusivities in nanoporous crystalline materials. *Phys. Chem. Chem. Phys.* **15,** 7994–8016 (2013).

58. Prigogine, I. *The End Of Certainty* (The Free Press, 1997).

59. Kärger, J., Petzold, M., Pfeifer, H., Ernst, S. & Weitkamp, J. Single-file diffusion and reaction in zeolites. *J. Catal.* **136,** 283–299 (1992).

60. Kukla, V. *et al.* NMR studies of single-file diffusion in unidimensional channel zeolites. *Science* **272,** 702–704 (1996).

61. Burada, P. S., Hänggi, P., Marchesoni, F., Schmid, G. & Talkner, P. Diffusion in confined geometries. *ChemPhysChem* **40,** 45–54 (2009).

62. Kärger, J. in *Adsorption and Diffusion* (eds Karge, H. G. & Weitkamp, J.) 329–366 (Springer, 2008).

63. Barrer, R. M. & Jost, W. A note on interstitial diffusion. *Trans. Faraday Soc.* **45,** 928–930 (1949).

64. Barrer, R. M. *Zeolites and Clay Minerals as Sorbents and Molecular Sieves* (Academic Press, 1978).

65. Kärger, J. Some remarks on the straight and cross coefficients of irreversible thermodynamics of surface flow and on the relation between diffusion and self-diffusion. *Surf. Sci.* **36,** 797–801 (1973).

66. Darken, L. S. Diffusion, mobility and their interrelation through free energy in binary metallic systems. *Trans. Am. Inst. Min. Met. Eng.* **175,** 184–175 (1948).

67. Chmelik, C. *et al.* Mass transfer in a nanoscale material enhanced by an opposing flux. *Phys. Rev. Lett.* **104,** 085902 (2010).

68. Park, K. S. *et al.* Exceptional chemical and thermal stability of zeolitic imidazolate frameworks. *Proc. Natl Acad. Sci. USA* **103,** 10186–10191 (2006).

69. Zhang, K., Lively, R. P., Zhang, C., Koros, W. J. & Chance, R. R. Investigating the intrinsic ethanol/water separation capability of ZIF-8: an adsorption and diffusion study. *J. Phys. Chem. C* **117,** 7214–7225 (2013).

70. Kärger, J. A study of fast tracer desorption in molecular sieve crystals. *AIChE J.* **28,** 417–423 (1982).

71. Kärger, J., Bülow, M., Millward, B. R. & Thomas, J. M. A phenomenological study of surface barriers in zeolites. *Zeolites* **6,** 146–150 (1986).

72. Caro, J., Bülow, M., Jobic, H., Kärger, J. & Zibrowius, B. Molecular mobility measurement of hydrocarbons in zeolites by NMR techniques. *Adv. Catal.* **39,** 351–414 (1993).

73. Wright, P. A. *et al.* Cation-directed syntheses of novel zeolite-like metalloaluminophosphates STA-6 and STA-7 in the presence of azamacrocycle templates. *J. Chem. Soc. Dalton Trans.* 1243–1248 (2000).

74. Castro, M. *et al.* Co-templating and modelling in the rational synthesis of zeolitic solids. *Chem. Commun.* 3470–3472 (2007).

75. Tzoulaki, D. *et al.* Assessing nanoporous materials by interference microscopy: remarkable dependence of molecular transport on composition and microstructure in the silicoaluminophosphate zeotype STA-7. *J. Am. Chem. Soc.* **132,** 11665–11670 (2010).

76. Pan, L. *et al.* Zn(tbip): a highly stable guest-free mircoporous metal organic framework with unique gas separation capability. *J. Am. Chem. Soc.* **128,** 4180–4181 (2006).

77. Tzoulaki, D. *et al.* Assessing surface permeabilities from transient guest profiles in nanoporous materials. *Angew. Chem. Int. Ed.* **48,** 3525–3528 (2009).

78. Hibbe, F. *et al.* The nature of surface barriers on nanoporous solids explored by microimaging of transient guest distributions. *J. Am. Chem. Soc.* **133,** 2804–2807 (2011).

79. Heinke, L. & Kärger, J. Correlating surface permeability with intracrystalline diffusivity in nanoporous solids. *Phys. Rev. Lett.* **106,** 074501 (2011).

80. Sholl, D. S. A porous maze. *Nature Chem.* **3,** 429–430 (2011).

81. Hibbe, F. *et al.* Monitoring molecular mass transfer in cation-free nanoporous host-crystals of type AlPO-LTA. *J. Am. Chem. Soc.* **134,** 7725–7732 (2012).

82. Sierra, L., Deroche, C., Gies, H. & Guth, J. L. Synthesis of new microporous AlPO$_4$ and substituted derivatives with the LTA structure. *Micropor. Mater.* **3,** 29–38 (1994).

83. Corma, A., Rey, F., Rius, J., Sabater, M. J. & Valencia, S. Supramolecular self-assembled molecules as organic directing agent for synthesis of zeolites. *Nature* **431,** 287–290 (2004).

84. Huang, A., Liang, F., Steinbach, F., Gesing. T. M. & Caro, J. Neutral and cation-free LTA-type aluminophosphate (AlPO$_4$) molecular sieve membrane with high hydrogen permselectivity. *J. Am. Chem. Soc.* **132,** 2140–2141 (2010).

85. Ruthven, D. M. in *Adsorption and Diffusion* (eds Karge, H. G. & Weitkamp, J.) 1–43 (Springer, 2008).

86. Ruthven, D. M. Diffusion in type A zeolites: new insights from old data. *Micropor. Mesopor. Mater.* **162,** 69–79 (2012).

87. Dudko, O. K., Berezhkovskii, A. M. & Weiss, G. H. Time-dependent diffusion coefficients in periodic porous materials. *J. Phys. Chem. B* **109,** 21296–21299 (2005).

88. Freund, H. J. in *Handbook of Heterogeneous Catalysis* 2nd edn, Vol. 2 (eds Ertl, G., Knözinger, H., Schüth, F. & Weitkamp, J.) 1375–1415 (Wiley-VCH, 2008).

89. Atkins, P. W. & de Paula, J. *Physical Chemistry* 8th edn (Oxford Univ. Press, 2006).

90. Chmelik, C. *et al.* Ensemble measurement of diffusion: novel beauty and evidence. *ChemPhysChem* **10,** 2623–2627 (2009).

91. Binder, T. *Mass Transport in Nanoporous Materials: New Insights from Micro-Imaging by Interference Microscopy* PhD thesis, Univ. Leipzig (2013).

92. Tzoulaki, D., Schmidt, W., Wilczok, U. & Kärger, J. Formation of surface barriers on silicalite-1 crystal fragments by residual water vapour as probed with isobutane by interference microscopy. *Micropor. Mesopor. Mater.* **110,** 72–76 (2008).

93. Chmelik, C. *et al.* Exploring the nature of surface barriers on MOF Zn(tbip) by applying IR microscopy in high temporal and spatial resolution. *Micropor. Mesopor. Mater.* **129,** 340–344 (2010).

94. Derouane, E. G. & Gabelica, Z. A novel effect of shape selectivity: molecular traffic control in zeolite ZSM-5. *J. Catal.* **65,** 486–489 (1980).

95. Neugebauer, N., Bräuer, P. & Kärger, J. Reactivity enhancement by molecular traffic control. *J. Catal.* **194,** 1–3 (2000).

96. Clark, L. A., Ye, G. T. & Snurr, R. Q. Molecular traffic control in a nanoscale system. *Phys. Rev. Lett.* **84,** 2893–2896 (2000).

97. Vaughan, P. A. The crystal structure of the zeolite ferrierite. *Acta Crystallogr.* **21,** 983–990 (1966).

98. Morris, R. E. *et al.* Synchrotron X-ray diffraction, neutron diffraction, ^{29}Si MAS-NMR, and computational study of the siliceous form of zeolite ferrierite. *J. Am. Chem. Soc.* **116,** 11849–11855 (1994).

99. Rakoczy, R. A. *et al.* Synthesis of large crystals of all-silica zeolite ferrierite. *Micropor. Mesopor. Mater.* **104,** 1195–1203 (2007).

100. Marthala, V. R. R. *et al.* Solvothermal synthesis and characterization of large-crystal all-silica, aluminum-, and boron-containing ferrierite zeolites. *Chem. Mater.* **23,** 2521–2528 (2011).

101. Kortunov, P. *et al.* Internal concentration gradients of guest molecules in nanoporous host materials: measurement and microscopic analysis. *J. Phys. Chem. B* **110,** 23821–23828 (2006).

102. Hibbe, F., Marthala, R., Chmelik, C., Weitkamp, J. & Kärger, J. Micro-imaging of transient guest profiles in nanochannels. *J. Chem. Phys.* **135,** 184201 (2011).

103. Hibbe, F. *Micro-Imaging Employed to Study Diffusion and Surface Permeation in Porous Materials* PhD thesis, Univ. Leipzig (2012).

104. Krishna, R. & van Baten, J. M. Mutual slowing-down effects in mixture diffusion in zeolites. *J. Phys. Chem. C* **113,** 13154–13156 (2010).

105. Caro, J., Noack, M. & Kolsch, P. Zeolite membranes: from the laboratory scale to technical applications. *Adsorption* **11,** 215–227 (2005).

106. Gücüyener, C., van den Bergh, J., Gascon, J. & Kapteijn, F. Ethane/ethene separation turned on its head: selective ethane adsorption on the metal-organic framework ZIF-7 through a gate-opening mechanism. *J. Am. Chem. Soc.* **132,** 17704–17706 (2010).

107. Ferey, G. & Serre, C. Large breathing effects in three-dimensional porous hybrid matter: facts, analyses, rules and consequences. *Chem. Soc. Rev.* **38,** 1380–1399 (2009).

108. Salles, F. *et al.* Transport diffusivity of CO_2 in the highly flexible metal-organic framework MIL-53(Cr): a combination of quasi-elastic neutron scattering measurements and molecular dynamics simulations. *Angew. Chem. Int. Ed.* **121,** 8485–8489 (2009).

109. Lincke, J. *et al.* A novel copper-based MOF material: synthesis, characterization and adsorption studies. *Micropor. Mesopor. Mater.* **142,** 62–69 (2011).

110. Van Koeningsveld, H., Tuinstra, F., van Bekkum, H. & Jansen, C. J. The location of p-xylene in a single crystal of zeolite H-ZSM-5 with a new, sorbate-induced, orthorhombic framework symmetry. *Acta Crystallogr. B* **45,** 423–431 (1989).

111. Fyfe, C. A., Kennedy, G. J., Schutter, C. T. de & Kokotailo, G. T. Sorbate-induced structural changes in ZSM-5 (silicalite). *J. Chem. Soc. Chem. Commun.* 541–542 (1984).

112. Fyfe, C. A., Strobl, H., Gies, H. & Kokotailo, G. T. High-resolution solid-state NMR investigation of the nature of the interaction between organic substrates and the zeolite ZSM-5 lattice. *Can. J. Chem.* **66,** 1942–1947 (1988).

113. Snurr, R. Q., Bell, A. T. & Theodorou, D. N. Prediction of adsorption of aromatic hydrocarbons in silicalite from grand canonical Monte Carlo simulations with biased insert-ions. *J. Phys. Chem.* **97,** 13742–13752 (1993).

114. Snurr, R. Q., Bell, A. T. & Theodorou, D. N. A hierarchical atomistic/lattice simulation approach for the prediction of adsorption thermodynamics of benzene in silicalite. *J. Phys. Chem.* **98,** 5111–5119 (1994).

115. Lee, C-K. & Chiang, A. S. T. Adsorption of aromatic compounds in large MFI zeolite crystals. *J. Chem. Soc. Faraday Trans.* **92,** 3445–3451 (1996).

116. Song, L., Sun, Z-L., Ban, H-Y., Dai, M. & Rees, L. V. C. Benzene adsorption in microporous materials. *Adsorption* **11,** 325–339 (2005).

117. Karwacki, L. *et al.* Morphology-dependent zeolite intergrowth structures leading to distinct internal and outer-surface molecular diffusion barriers. *Nature Mater.* **8,** 959–965 (2009).

118. Kärger, J. Random walk through two-channel networks: a simple means to correlate the coefficients of anisotropic diffusion in ZSM-5 type zeolite. *J. Phys. Chem.* **95,** 5558–5560 (1991).

119. Yaghi, O. M. *et al.* Reticular synthesis and the design of new materials. *Nature* **423,** 705–714 (2003).

120. Na, K. *et al.* Directing zeolite structures into hierarchically nanoporous architectures. *Science* **333,** 328–332 (2011).

121. Ikezoe, Y., Washino, G., Uemura, T., Kitagawa, S. & Matsui, H. Autonomous motors of a metal–organic framework powered by reorganization of self-assembled peptides at interfaces. *Nature Mater.* **11,** 1081–1085 (2012).

122. Kärger, J. *Leipzig, Einstein, Diffusion* 2nd edn (Leipziger Universitätsverlag, 2010).

Additional information

Reprints and permissions information is available online at www.nature.com/reprints. Correspondence and requests for materials should be addressed to J.K.

Competing financial interests

The authors declare no competing financial interests.